Journal of Materials Chemistry A

PAPER

View Article Online
View Journal | View Issue

Cite this: J. Mater. Chem. A, 2014, 2, 5928

A fluorene based covalent triazine framework with high CO_2 and H_2 capture and storage capacities†

Stephan Hug,[abc] Maria B. Mesch,[d] Hyunchul Oh,[e] Nadine Popp,[d] Michael Hirscher,[e] Jürgen Senker[d] and Bettina V. Lotsch*[abc]

Received 28th December 2013
Accepted 4th February 2014

DOI: 10.1039/c3ta15417c

www.rsc.org/MaterialsA

Porous organic polymers have come into focus recently for the capture and storage of postcombusted CO_2. Covalent triazine frameworks (CTFs) constitute a nitrogen-rich subclass of porous polymers, which offers enhanced tunability and functionality combined with high chemical and thermal stability. In this work a new covalent triazine framework based on fluorene building blocks is presented, along with a comprehensive elucidation of its local structure, porosity, and capacity for CO_2 capture and H_2 storage. The framework is synthesized under ionothermal conditions at 300–600 °C using $ZnCl_2$ as a Lewis acidic trimerization catalyst and reaction medium. Whereas the materials synthesized at lower temperatures mostly feature ultramicropores and moderate surface areas as probed by CO_2 sorption (297 $m^2\ g^{-1}$ at 300 °C), the porosity is significantly increased at higher synthesis temperatures, giving rise to surface areas in excess of 2800 $m^2\ g^{-1}$. With a high fraction of micropores and a surface area of 1235 $m^2\ g^{-1}$, the CTF obtained at 350 °C shows an excellent CO_2 sorption capacity at 273 K (4.28 mmol g^{-1}), which is one of the highest observed among all porous organic polymers. Additionally, the materials have CO_2/N_2 selectivities of up to 37. The hydrogen adsorption capacity of 4.36 wt% at 77 K and 20 bar is comparable to that of other POPs, yet the highest among all CTFs studied to date.

Introduction

Lately, the development of covalent triazine frameworks (CTFs), a subclass of porous organic polymers (POPs), garnered significant attention owing to their high surface areas combined with a highly robust nature, that is, high thermal (>300 °C) and chemical stabilities towards concentrated acids and bases.[1–5] Therefore, CTFs are considered ideal scaffolds for applications such as heterogeneous catalysis,[6–9] gas storage and separation.[9–16] Recently, low temperature syntheses of CTFs have set the stage for further applications such as for chemo- and size-selective membranes[17] and in optoelectronics.[10]

The development of potent gas storage systems has been fueled by the need for highly selective gas capture materials apt to selectively filter out or enrich relevant gases such as methane or carbon dioxide. The anthropogenic emission of CO_2 is known to be a major source of global warming. The global emission of CO_2 by power plants and public transportation has risen remarkably in the last decades.[18] According to the International Energy Agency (IEA), appropriate capture and storage of post-combusted CO_2 (CCS) has the potential of decreasing the emissions up to 20%.[19] Typically, flue gas of a coal-fired power plant consists of approximately 15% CO_2, 5% H_2O, 5% O_2 and 75% N_2 and is emitted at 40–80 °C and 1 bar.[20,21] Therefore, materials suitable for CCS require a high preference for adsorption of CO_2 under these conditions. Amine scrubbing and cryogenic cooling are the only established technologies for CO_2 capture up to date, which, however, have the disadvantage of increasing the energy requirements of a power plant by 25–40%.[20,22] Especially amine scrubbing needs large volumes of solvents, high temperatures for regeneration and costly disposal when expired.[22,23] The disposal and the formation of toxic byproducts during the regeneration step additionally raise environmental concerns about this technology. Lately, the use of solid physical adsorbents for CO_2 capture, such as metal–organic frameworks (MOFs) and POPs, was part of several reviews.[20,21,24–27] Main advantages of solid adsorbents are their

[a]Department of Chemistry, Ludwig-Maximilians-Universität München, Butenandtstr. 5-13, 81377 Munich, Germany. E-mail: bettina.lotsch@cup.uni-muenchen.de; Fax: +49 89 2180 77440; Tel: +49 89 2180 77429
[b]Max Planck Institute for Solid State Research, Heisenbergstr. 1, 70569 Stuttgart, Germany. E-mail: b.lotsch@fkf.mpg.de; Fax: +49 711 689 1612; Tel: +49 711 689 1610
[c]Nanosystems Initiative Munich (NIM) and Center for Nanoscience, Schellingstr. 4, 80799 Munich, Germany
[d]Inorganic Chemistry III, Universität Bayreuth, Universitätsstr. 30, 95447 Bayreuth, Germany
[e]Max Planck Institute for Intelligent Systems, Heisenbergstr. 3, 70569 Stuttgart, Germany

† Electronic supplementary information (ESI) available: Temperature programs, elemental analysis, XRD patterns, ^{13}C ssNMR of *fl*-CTF500, ^{15}N ssNMR of tris(9*H*-fluoren-2-yl)-1,3,5-triazine, CPPI analysis, Ar isotherm of *fl*-CTF300, BET plots, Ar-QSDFT fittings, CO_2-NLDFT distributions and fittings, CO_2 isotherms at 298 and 313 K, H_2 isotherms at 298 and 20 K, H_2 Q_{st} plot, N_2 isotherms at 298 K, Henry and IAST calculations, ^1H and ^{13}C NMR spectra of 9*H*-fluorene-2-carbonitrile and 9*H*-fluorene-2,7-dicarbonitrile, and DTA/TG measurements. See DOI: 10.1039/c3ta15417c

long lifetimes and recovery at moderate temperatures. Especially POPs are promising because of their high chemical and thermal stabilities as well as synthetic versatility, giving rise to a large variety of functional and structural designs.

In this work we present the synthesis and characterization of a new fluorene-based covalent triazine framework (*fl*-CTF) at different temperatures. We tested the material properties regarding CO_2 adsorption at 273 K, 298 K and 313 K, along with the CO_2 over N_2 selectivity, showing high capture capacities and good selectivities. Additionally, we measured high-pressure adsorption of H_2 at 77 K and 298 K, yielding uptakes at the forefront of polymeric hydrogen storage systems.

Experimental section

Materials and methods

All starting materials and solvents were obtained from commercial sources and were used without further purification. 2,7-Dibromo-9*H*-fluorene (99%) was purchased from Acros Organics. Zinc cyanide (98%) and trifluoromethanesulphonic acid (99%) were obtained from ABCR. Anhydrous zinc chloride (99.995%), 2-bromo-9*H*-fluorene (95%) and tetrakis(triphenylphosphine)palladium(0) (99%) were purchased from Sigma Aldrich. Dimethylformamide (99%) and 1,5-bis(diphenyl-phosphino)pentane (97%) were obtained from Alfa Aesar.

Argon, carbon dioxide and nitrogen adsorption/desorption measurements were performed at 87, 273, 298 and 313 K with an Autosorb iQ surface analyzer (Quantachrome Instruments, USA). Samples were outgassed in a vacuum (10^{-7} mbar) at 200–300 °C for 6 h to remove all guests. Pore-size distributions were determined using the calculation model for Ar at 87 K on carbon (slit pore, QSDFT equilibrium model) or for CO_2 at 273 K on carbon (NLDFT model) of the ASiQwin software (v2.0) from Quantachrome. For BET calculations pressure ranges of the Ar isotherms were chosen with the help of the BET Assistant in the ASiQwin software. In accordance with the ISO recommendations multipoint BET tags equal or below the maximum in $V(1 - P/P_0)$ were chosen. The isosteric heats of adsorption were calculated from the CO_2 adsorption isotherms using the Quantachrome software ASiQwin (v2.0) based on the Clausius–Clapeyron equation (see ESI,† section 6c).

High-pressure hydrogen adsorption/desorption measurements were performed on an automated Sievert's type apparatus (PCTPro-2000) with a so-called micro-doser (MD) from HyEnergy. The original setup was upgraded by a heating and cooling device to regulate the sample temperature. The adsorption and desorption isotherms (0–20 bar) were measured at various temperatures (77 to 298 K) in a sample cell volume of ≈1.3 mL using ultra high purity hydrogen gas (99.999%). Samples were outgassed in a vacuum (4.5×10^{-6} mbar) at 200 °C for 6 h to remove all guests. The isosteric heat of adsorption is calculated from the absolute adsorbed hydrogen according to a variant of the Clausius–Clapeyron equation (see ESI†).

Cryogenic hydrogen adsorption/desorption measurements at 19.5 K were measured with laboratory-designed volumetric adsorption equipment with a temperature controlled cryostat. The experimental set-up has been described in detail elsewhere.[28,29] Samples were activated under vacuum (10^{-4} mbar) at 150 °C for 12 h, prior to each measurement. For the laboratory-designed cryostat, the temperature control was calibrated by measuring the liquefaction pressure for hydrogen and nitrogen in the empty sample chamber at various temperatures.

Infrared (IR) spectroscopy measurements were carried out on a Perkin Elmer Spectrum BX II (Perkin Elmer, USA) with an attenuated total reflectance unit.

Powder X-ray diffraction (XRD) was measured on a BRUKER D8 Advance (Bruker AXS, Madison, Wisconsin, USA) in the Bragg–Brentano geometry or on a HUBER G670 (HUBER Diffraktionstechnik, Rimsting, Germany) in the Guinier geometry equipped with an imaging plate detector.

Elemental analysis (EA) was carried out with an Elementar vario EL (Elementar Analysensysteme, Germany).

Magic angle spinning (MAS) solid-state nuclear magnetic resonance (ssNMR) spectra were recorded at ambient temperature on a BRUKER DSX500 Avance NMR spectrometer or a BRUKER AvanceIII HD 400 NMR spectrometer (Bruker Biospin, Rheinstetten, Germany) with an external magnetic field of 11.75 T and 9.4 T, respectively. The operating frequencies are 500.1 MHz, 125.7 MHz and 400.1 MHz, 100.6 MHz for ^{1}H and ^{13}C, respectively and the spectra were referenced relative to TMS (^{1}H, ^{13}C). The samples were contained either in 2.4, 3.2 mm or 4 mm ZrO_2 rotors. The 1D $^{1}H^{13}C$ cross-polarization (CP) MAS spectra were acquired with a ramped-amplitude (RAMP) CP sequence and contact times between 2 and 10 ms. CPPI (cross-polarization combined with polarization inversion) experiments were carried out to get information about the number of hydrogen atoms directly attached to the carbon. An initial contact time of 2 ms was used and spectra with inversion times up to 400 μs were measured. The measurements were carried out using spinning frequencies of 10 kHz and 15 kHz for CP, and 5.1 kHz for CPPI measurements, respectively. During acquisition broadband proton decoupling using SPINAL64 or TPPM was carried out.

Solution-state NMR spectroscopy was performed on a JEOL DELTA NMR (JEOL, Japan) by single pulse experiments. The spectra were referenced against $CDCl_3$ ($\delta(^{1}H)$ 7.26 ppm, $\delta(^{13}C\{^{1}H\})$ 77.16 ppm).

High resolution mass spectroscopy (HRMS) was carried out on a JEOL MS700 (JEOL, Japan), by direct electron ionization (DEI).

Differential thermal analysis and thermogravimetry (DTA/TG) were measured on a SETARAM TG-DTA92-2400 combined DTA-TG-thermobalance (SETARAM Instrumentation, France) in aluminum oxide crucibles. Heating was performed from room temperature to 800 °C with a heating rate of 5 °C min^{-1} under a helium atmosphere.

Microwave reactions were carried out in a Biotage Initiator (Biotage AB, Sweden) in 10–20 mL microwave vials from Biotage.

9*H*-Fluorene-2-carbonitrile[30]

A microwave vial was charged with DMF (20.0 mL) and a stream of argon was bubbled through the solvent for 30 min. 2-Bromo-9*H*-fluorene (1.03 g, 4.00 mmol), $Zn(CN)_2$ (939 mg, 8.00 mmol),

$Pd(PPh_3)_4$ (185 mg, 0.16 mmol), and bis(diphenyl-phosphino) pentane (72.7 mg, 0.16 mmol) were added and the stream of argon was continued for 2 min. The vial was sealed and the yellow mixture was heated in the microwave for 5 min at 150 °C. The obtained orange suspension was poured into sat. $NaHCO_3$-sol. (200 mL) and extracted with $CHCl_3$ (3 × 200 mL). The combined organic layers were dried over $MgSO_4$ and concentrated *in vacuo*. The crude product was purified by column chromatography (hexane–ethylacetate 95 : 5) to yield 9*H*-fluorene-2-carbonitrile as a light tanned solid (0.59 g, 3.09 mmol, 77%). δ_H (300 MHz; $CDCl_3$) 7.86–7.79 (3H, m, Ph), 7.68–7.64 (1H, m, Ph), 7.67–7.57 (1H, m, Ph), 7.47–7.37 (2H, m, Ph), 3.93 (2H, s, CH_2); δ_C (68 MHz; $CDCl_3$) 146.3, 144.0, 143.7, 140.0, 131.3, 128.72, 128.68, 127.4, 125.4, 121.1, 120.5, 119.8, 109.8, 36.9.

9*H*-Fluorene-2,7-dicarbonitrile[31]

A microwave vial was charged with DMF (20.0 mL) and a stream of argon was bubbled through the solvent for 30 min. 2,7-Dibromo-9*H*-fluorene (1.31 g, 4.00 mmol), $Zn(CN)_2$ (939 mg, 8.00 mmol), $Pd(PPh_3)_4$ (277 g, 0.24 mmol), and bis(diphenyl-phosphino)pentane (109 mg, 0.24 mmol) were added and the stream of argon was continued for 2 min. The vial was sealed and the yellow mixture was heated in the microwave for 5 min at 150 °C. The obtained orange suspension was poured into H_2O (300 mL) and extracted with $CHCl_3$ (4 × 300 mL). The combined organic layers were dried over $MgSO_4$ and concentrated *in vacuo*. The crude product was recrystallized from CH_2Cl_2 to give 9*H*-fluorene-2,7-dicarbonitrile as light green crystals (0.66 g, 3.05 mmol, 76%). δ_H (270 MHz; $CDCl_3$) 7.93 (2H, d, $^3J_{HH} = 8.1$ Hz, Ph), 7.89 (2H, d, $^4J_{HH} = 0.7$ Hz, Ph), 7.74 (2H, dd, $^3J_{HH} = 8.0$ Hz, $^4J_{HH} = 0.7$ Hz, Ph), 4.04 (2H, s, CH_2); δ_C (68 MHz; $CDCl_3$) 144.4, 144.3, 131.7, 129.1, 121.7, 119.1, 111.8, 36.9.

Tris(9*H*-fluoren-2-yl)-1,3,5-triazine

In an outgassed 25 mL Schlenk tube trifluoromethanesulphonic acid (0.80 mL, 9.00 mmol) was cooled to −18 °C and under stirring 9*H*-fluorene-2-carbonitrile (574 mg, 3 mmol) was added in portions. The mixture was left in the icebath for 40 h giving a dark green solid. The solid was slowly added to ice, turning into an orange suspension. After neutralizing with ammonia (25% in H_2O) the suspension turned light purple and the precipitate was filtered off. Washing with water and little amounts of acetone yielded tris(9*H*-fluoren-2-yl)-1,3,5-triazine as a light tanned solid (477 mg, 83%). MS (DEI+) *m*/*z* (relative intensity) 574 (MH^+, 18%), 573 (M^+, 40), 192 ($C_{14}H_{10}N^+$, 100), 191 ($C_{14}H_9N^+$, 92), 190 ($C_{14}H_8N^+$, 79), 165 ($C_{13}H_9^+$, 24), 164 ($C_{13}H_8^+$, 21). HRMS (DEI) *m*/*z*: $[M]^+$ calcd for $C_{42}H_{27}N_3$ 573.2205; found 573.2219. Anal. calc. for $C_{42}H_{27}N_3$: C, 87.93; H, 4.74; N, 7.32. Found: C, 86.69; H, 4.86; N, 7.18%. Mp 350–356 °C (decomp.).

Synthesis of covalent triazine frameworks

In a typical synthesis a Duran ampoule (1.5 × 12 cm) was charged with 9*H*-fluorene-2,7-dicarbonitrile (500 mg, 2.31 mmol) and $ZnCl_2$ (1.57 g, 11.6 mmol) within a glove box. The ampoule was flame sealed under vacuum and was subjected in a tube oven to temperatures between 300 and 600 °C (for temperature programs, see Table S1, ESI†). After cooling to ambient temperature, the ampoule was opened and its content ground thoroughly. The crude product was stirred in H_2O (150 mL) for 1 h, filtered, and washed with 1 M HCl (75 mL) and ethanol (75 mL). The mixture was then stirred at 90 °C in 1 M HCl (80 mL) overnight, filtered, and subsequently washed with 1 M HCl (3 × 75 mL), H_2O (12 × 75 mL), THF (2 × 75 mL), and acetone (1 × 75 mL). Finally, the black powder was dried overnight at 60 °C.

Results and discussion

Synthesis and characterization

The standard procedure for preparing CTFs is by ionothermal synthesis using $ZnCl_2$ both as a "solvent" and as a Lewis acidic catalyst at temperatures above 300 °C.[1–4] CTFs synthesized at low temperatures (300–400 °C) may show little crystallinity, yet at the same time may have well-defined local structures.[1,5,9,32] Synthesis at higher temperatures typically leads to dramatic increases in the surface areas accompanied by the loss of structural elements, especially the triazine moieties.[4,5] In this work we followed this procedure using 9*H*-fluorene-2,7-dicarbonitrile as a precursor. The precursor was synthesized by a Negishi crosscoupling reaction from 2,7-dibromo-9*H*-fluorene in the microwave with just 5 min reaction time (Scheme 1). This straightforward method to produce aromatic dinitriles is analogous to the synthesis described by us previously.[5] Work-up was done by recrystallisation and gave good yields of 76%. The syntheses of the CTFs were performed at temperatures between 300 and 600 °C, yielding fluorene-CTFs at 300 °C (*fl*-CTF300), 350 °C (*fl*-CTF350), 400 °C (*fl*-CTF400), 500 °C (*fl*-CTF500) and 600 °C (*fl*-CTF600). The reaction times were 48 h for all samples, except for *fl*-CTF300 and *fl*-CTF350, where the reaction times were raised to 96 h after very low yields had been obtained due to unreacted monomers or oligomers. Reaction times of 168 h did not give higher yields or changes in the material properties.

CTF-0, CTF-1 and CTF-2 are the only three examples of CTFs which show moderate crystallinity.[1,12,32] Therefore, it was little surprising that our materials were found to be largely amorphous in the XRD measurements, except for broad peaks at 14.8, 22.7 and 33.6° 2θ. The peak at 22.7° 2θ is attributed to a 00*l* reflection indicating a "graphitic" layer stacking with an interlayer distance of ~3.9 Å, which is rather large and consistent with only weak interlayer coupling (Fig. S1, ESI†).

To probe whether trimerization in these samples was completed with the fluorene units still being intact, we used IR spectroscopy and ssNMR measurements and compared the results with the model compound tris(9*H*-fluoren-2-yl)-1,3,5-triazine. Fig. 1 depicts the IR and Fig. 2 and S2† the ^{13}C ssNMR spectra of the as-synthesized materials. *fl*-CTF300 shows well resolved signals in the IR spectrum, whereas the signals weaken at higher synthesis temperatures and are flattened out to a large extent for *fl*-CTF600, indicating graphitization of the networks. This is confirmed by the ^{13}C ssNMR measurements, which show a broadening and weakening of the signals with rising temperatures. Remarkably, the NMR spectrum of *fl*-CTF600

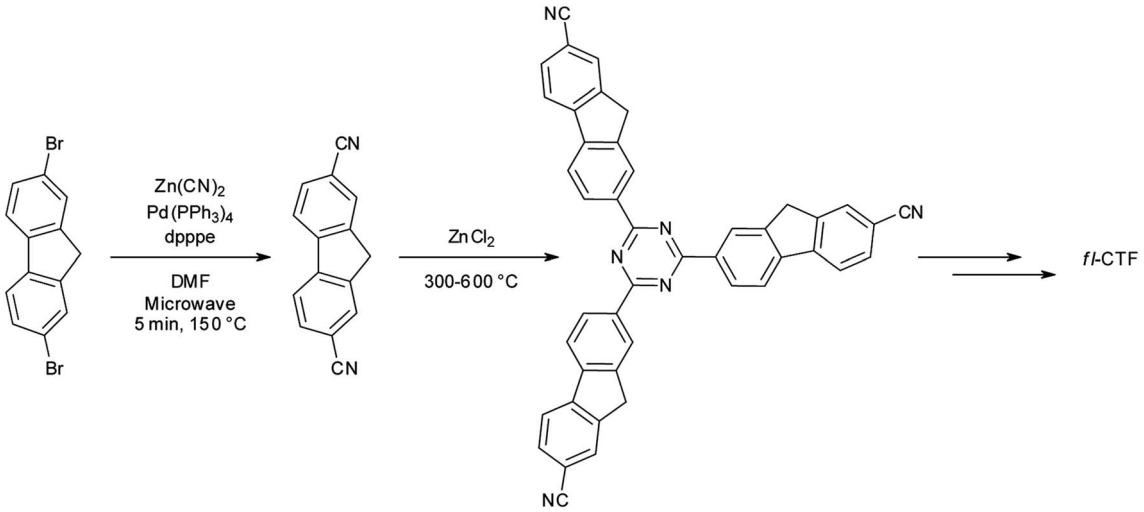

Scheme 1 Synthesis route for *fl*-CTFs.

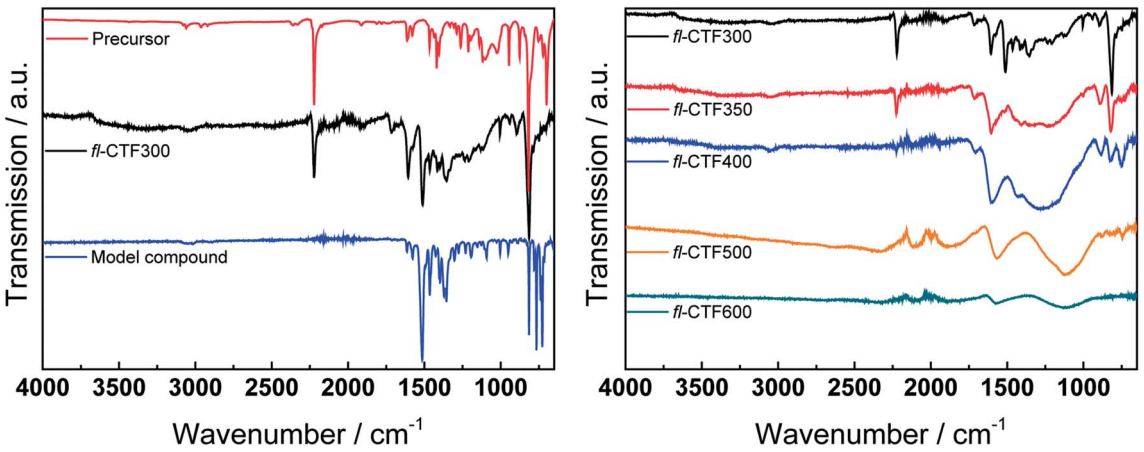

Fig. 1 (Left) IR spectra of 9*H*-fluorene-2,7-dicarbonitrile, *fl*-CTF300 and tris(9*H*-fluoren-2-yl)-1,3,5-triazine. (Right) IR spectra of the samples *fl*-CTF300, *fl*-CTF350, *fl*-CTF400, *fl*-CTF500 and *fl*-CTF600.

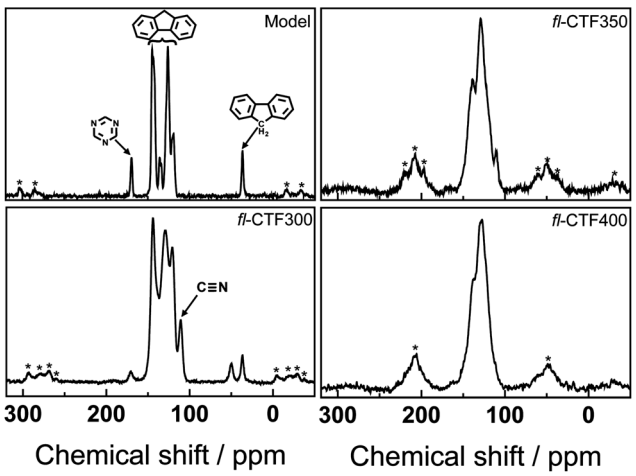

Fig. 2 ^{13}C MAS ssNMR spectra of tris(9*H*-fluoren-2-yl)-1,3,5-triazine (top left), *fl*-CTF300 (bottom left), *fl*-CTF350 (top right) and *fl*-CTF400 (bottom left). Asterisks mark rotational side bands.

could not be measured owing to the high degree of graphitization. The IR and ssNMR spectra of *fl*-CTF300 and *fl*-CTF350 show the presence of a nitrile band (2223 cm^{-1}, 109.5 ppm), indicating that there are still unreacted nitrile groups in the polymer. Those signals are not visible at higher synthesis temperatures. The strong IR band in the *fl*-CTF300 spectrum at 1511 cm^{-1} can be assigned to the C–N stretching mode of the triazine ring,[32,33] whereas the band at 1352 cm^{-1} is due to in-plane triazine ring stretching vibrations.[3,34] This and the corresponding NMR shift at 168.6 ppm evidence successful formation of the triazine moieties (Fig. 2, bottom left). The signals between 144 and 118 ppm and the peak at 36.9 ppm belong to the fluorene unit, which accordingly stays intact at 300 °C. The signal at 50 ppm is assigned to a sp^3 CH group, which was corroborated by a CPPI measurement (Fig. S4†). This resonance suggests the formation of 9,9′-bifluorenyl units *via* crosslinking. A broadening of the bands between 1500 and 1100 cm^{-1} and the decrease of the triazine bands in the IR

spectrum of *fl*-CTF350 indicates commencing degradation of the system. Again, ssNMR measurements confirm these results. The bands at 1607 and 814 cm^{-1} appear both in the precursor and in *fl*-CTF300 and can hence likely be assigned to the fluorene species. These bands are still retained in the spectra of *fl*-CTF350 and *fl*-CTF400, indicating intact fluorene units in those samples. The spectra of *fl*-CTF500 and *fl*-CTF600 do not show the fluorene signature anymore, which confirms the ongoing degradation of the system at elevated temperatures.

In summary, both IR spectroscopy and ssNMR measurements indicate degradation of the networks at temperatures higher than 300 °C, which is in line with observations made for all synthesized CTFs so far. Temperatures in excess of 400 °C are not tolerated by the triazine rings and likely induce retro-trimerization reactions with subsequent rearrangements, giving rise to irreversible formation of C–C bonds accompanied by a loss of N_2.

To gain more information about the degree and course of degradation, we utilized EA measurements. EA data shown in Table S2† reveal a trend which is very similar to many synthesized CTFs: by raising the synthesis temperature, the nitrogen and hydrogen content decreases and the carbon content increases. The loss of nitrogen is very significant with a nitrogen loss of more than 40% for *fl*-CTF600 compared to *fl*-CTF300. Notably, the nitrogen content of *fl*-CTF300 is already lower than the calculated value, thus confirming the IR results, which reveal smaller amounts of triazine compared to the model compound.

To confirm the thermal stability of the materials we carried out DTA/TG measurements on the samples *fl*-CTF300 and *fl*-CTF600. The results (Fig. S25 and S26†) show degradation temperatures close to the synthesis temperatures and a rather low weight loss, especially for the *fl*-CTF600 sample.

Porosity measurements

Although an increase in the synthesis temperature leads to materials with less local order and nitrogen content, it typically entails materials with higher surface areas (SAs).[2,3,5] The porosities of the *fl*-CTFs were determined by argon and carbon dioxide physisorption measurements. Fig. 3 (left) shows the argon isotherms of the samples *fl*-CTF350, *fl*-CTF400, *fl*-CTF500 and *fl*-CTF600. It should be mentioned that *fl*-CTF300 (Fig. S6†) adsorbed only small amounts of argon and therefore showed overall poor porosity. The isotherm of *fl*-CTF350 is typical for microporous materials in that it shows rapid argon uptake at low relative pressures ($p\,p_0^{-1} < 0.05$). Nevertheless, it cannot be described as a type I isotherm because of continuous adsorption of argon at higher pressures, indicating additional mesoporosity with a broad mesopore size distribution and a hysteresis almost spanning the entire range of $p\,p_0^{-1} = 0$–0.9. The hysteresis resembles type H4, typical for materials with slit-shaped pores. The low pressure character of the hysteresis indicates pores within the size range of the adsorbate, causing delayed desorption.[35] The isotherm of *fl*-CTF400 shows rapid argon adsorption at low relative pressures as well. The continuous adsorption at higher relative pressures is higher than in *fl*-CTF350, which should be ascribed to an increased fraction of mesopores. The isotherms of *fl*-CTF500 and *fl*-CTF600 show similar shapes and can be described as a combination of isotherms of type I and IV. The micropore filling is followed by mesopore filling showing a type H2 hysteresis around $p\,p_0^{-1} = 0.4$. H2 hystereses describe systems with rather ill-defined pore sizes and shapes and are often observed for amorphous materials.

The SAs of the materials were calculated from the isotherms based on the BET model and are listed in Table 1.[36] The highest SA of 2862 $m^2\ g^{-1}$ is found for *fl*-CTF400, which is the third highest for all CTFs after CTF-1 (400/600 °C, 3270 $m^2\ g^{-1}$)[2] and bipy-CTF (700 °C, 3219 $m^2\ g^{-1}$).[5] For *fl*-CTF500 and *fl*-CTF600 the values decrease, which is unexpected, since for all published CTFs a rise in synthesis temperature showed an increase in the SA, accompanied by a continuous decomposition of the materials ("foaming"). This phenomenon can be explained by the pore size distribution of the materials which was calculated by QSDFT methods (Fig. 3, right). For *fl*-CTF350 mainly micropores are observed with two main peaks at 1.05 and 0.5 nm. The latter indicates pores smaller than 0.5 nm (ultramicropores), which

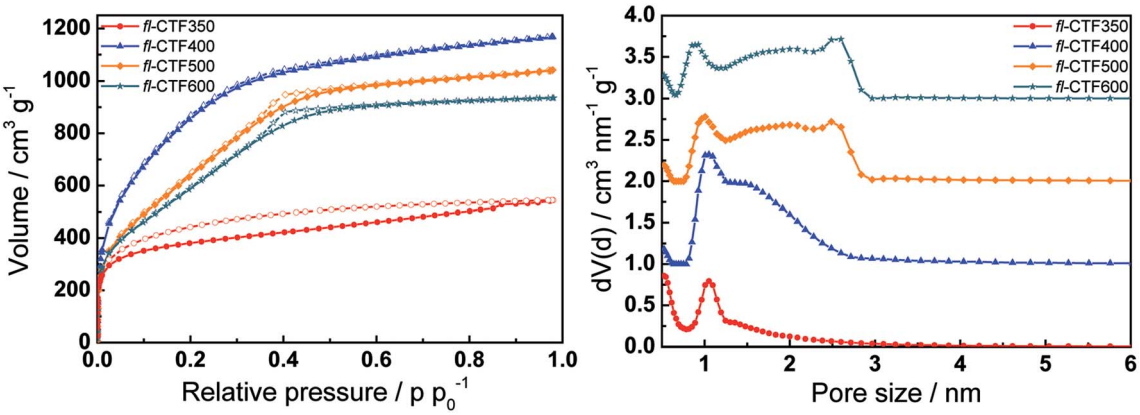

Fig. 3 (Left) Argon adsorption (filled symbols) and desorption (open symbols) isotherms at 87 K of *fl*-CTF350, *fl*-CTF400, *fl*-CTF500 and *fl*-CTF600. (Right) Pore size distributions of *fl*-CTF350, *fl*-CTF400, *fl*-CTF500 and *fl*-CTF600 from DFT calculations. The curves are shifted vertically in steps of 1 $cm^3\ nm^{-1}\ g^{-1}$.

Table 1 BET surface areas, CO_2 and N_2 uptakes, heats of adsorption and CO_2/N_2 selectivities of *fl*-CTFs

		Pore volume [$cm^3\ g^{-1}$]			CO_2 uptake[a] [mmol g^{-1}]					Selectivity[d]	
Sample	BET SA [$m^2\ g^{-1}$]	$V_{Ar,mic,DFT}$[e]	$V_{Ar,tot,DFT}$[f]	$V_{Ar,mic,DFT}/V_{Ar,tot,DFT}$	273 K	298 K	313 K	N_2 uptake[b] [mmol g^{-1}]	Q_{st}[c] [kJ mol^{-1}]	Henry	IAST
fl-CTF300	15	—	—	—	1.27	0.71	0.42	0.04	43.1	35	37
fl-CTF350	1235	0.57	0.67	0.85	4.28	2.29	1.59	0.18	32.7	27	23
fl-CTF400	2862	1.13	1.45	0.78	4.13	1.97	1.31	0.17	30.7	15	16
fl-CTF500	2322	0.77	1.29	0.60	3.26	1.65	1.11	0.21	31.7	13	12
fl-CTF600	2113	0.70	1.16	0.60	3.48	1.80	1.22	0.22	32.4	14	12

[a] At 1 bar. [b] At 1 bar and 298 K. [c] At zero coverage. [d] At 298 K. [e] Pore volume for pores smaller than 2 nm calculated from the Ar QSDFT model. [f] Total pore volume from the Ar QSDFT model.

are not observable by argon measurements. For *fl*-CTF400 the peak at 1.05 nm increases and additionally a wide distribution of pores from 1.2 to 3 nm is observed, with mainly pores in the micropore region. *fl*-CTF500 and *fl*-CTF600 show comparable distributions, with an additional peak around 2.5 nm, which can be assigned to small mesopores. Overall, an increasingly mesoporous character with rising synthesis temperature is typical for CTFs, yet normally the increasing amount of mesopores is not accompanied by a significant decrease of the micropores.[2,5]

The amount of micropores compared to mesopores can be calculated by the ratio of the microporous volume V_{mic} to the total pore volume V_{tot}. These pore volumes can be calculated from the amount of vapor adsorbed at chosen relative pressures assuming the pores are filled with a liquid adsorbate, and from DFT calculations. The results for the *fl*-CTFs are listed in Tables 1 and S4† and confirm the previous observations. *fl*-CTF400 features the largest absolute amount of micropores followed by *fl*-CTF500 and *fl*-CTF600. Remarkably, *fl*-CTF350 has the highest fraction of micropores with respect to the total pore volume (85%), which is clearly higher than for *fl*-CTF500 and *fl*-CTF600 (both 60%). The widening of the pores can favorably be explained by the degradation of the networks at elevated synthesis temperatures, leading to a "swelling" ("foaming") of the materials.

The pore size distributions of the *fl*-CTFs indicate ultramicropores, which cannot be detected by argon measurements, but by carbon dioxide physisorption measurements, which allow us to probe pore sizes down to ≈0.35 nm. The isotherms shown in Fig. 4 have comparable shapes, which is consistent with the literature. In contrast to its non-porous character established by Ar physisorption, *fl*-CTF300 adsorbs moderate amounts of CO_2, which can be rationalized by the presence of pores that are accessible to CO_2 but not to Ar. A comparable phenomenon is observed for *fl*-CTF350, which adsorbs more CO_2 than all other *fl*-CTFs, although having around half as much accessible SA as determined by argon physisorption. The accessible CO_2 SAs were calculated with DFT simulations and are shown in Table S6.† The values are much lower than those for argon measurements, since the calculations only take pores smaller than 1.45 nm into account. Nevertheless, *fl*-CTF300 shows a SA of 297 $m^2\ g^{-1}$ which is nearly half as much as that of

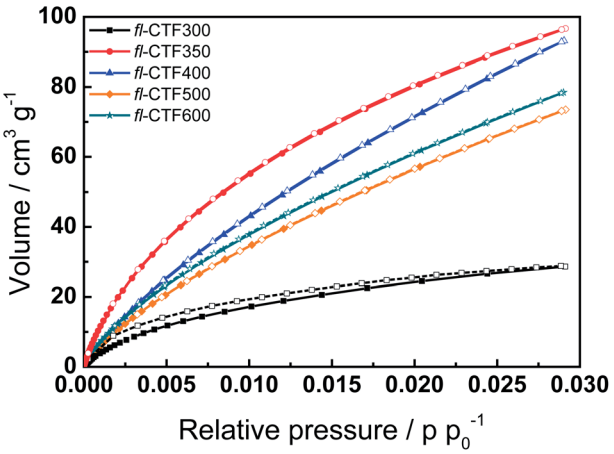

Fig. 4 Carbon dioxide adsorption (filled symbols) and desorption (open symbols) isotherms at 273 K of *fl*-CTF300, *fl*-CTF350, *fl*-CTF400, *fl*-CTF500 and *fl*-CTF600.

fl-CTF500 and *fl*-CTF600. The highest SA is observed for *fl*-CTF400, followed by *fl*-CTF350. All samples show a broad pore size distribution ranging from 0.35–1.00 nm (Fig. S16†). A hydrogen physisorption measurement at 20 K validated the SA of *fl*-CTF400 giving a BET SA of 2829 $m^2\ g^{-1}$ (Fig. S12 and S13†).

Gas storage and selectivity studies

The high capacities of the *fl*-CTFs for CO_2 sorption at 273 K are promising for the usage as CCS materials. Therefore, temperature-dependent sorption studies at 298 and 313 K were carried out and the heats of adsorption were calculated (Fig. 5).

The uptakes at 1 bar and the heats of adsorption at zero coverage are summarized in Table 1. With 4.28 mmol g^{-1} at 273 K *fl*-CTF350 shows the highest uptake of all materials. This value is lower than that of recently reported FCTF-1 (4.67–5.53 mmol g^{-1}),[16] but higher than the reported values for all other CTFs such as CTF-0 (4.22 mmol g^{-1}),[9] CTF-1 (2.47–3.82 mmol g^{-1}),[16] CTF-P2–P6 (1.88–3.39 mmol g^{-1}),[10] CTF-P1M–P6M (0.94–4.20 mmol g^{-1}),[10] MCTF300–500 (2.25–3.16 mmol g^{-1}),[12] PCTF-1–7 (1.84–3.23 mmol g^{-1})[11,15] and TPI-1–7 (0.68–2.45 mmol g^{-1}).[34] In addition, they are higher than the uptake capacities of numerous POPs such as covalent organic

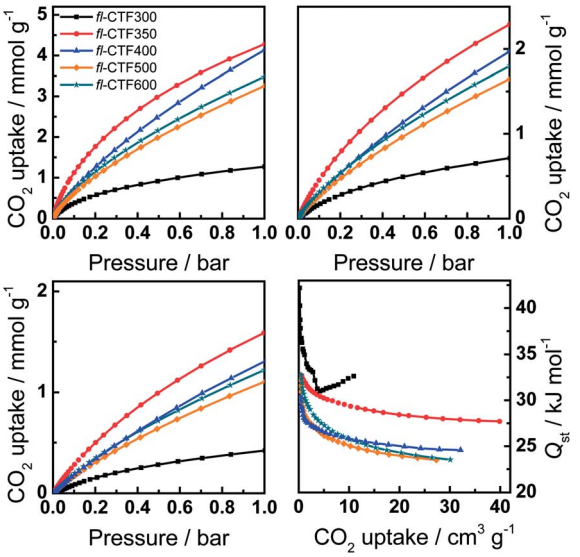

Fig. 5 Carbon dioxide adsorption isotherms of *fl*-CTF300, *fl*-CTF350, *fl*-CTF400, *fl*-CTF500 and *fl*-CTF600 at 273 K (top left), 298 K (top right), 313 K (bottom left) and corresponding heats of adsorption (bottom right).

frameworks (COFs; 1.21–3.86 mmol g^{-1}),[37,38] microporous polyimides (MPIs; 2.25–3.81 mmol g^{-1}),[39] and hyper-cross-linked organic polymers (HCPs; 1.91–3.92 mmol g^{-1})[40,41] (for an expanded list see Table S7†). Higher values were reported so far for benzimidazole-linked polymers (BILPs; 2.91–5.34 mmol g^{-1}),[42–44] and porous polymer frameworks (PPFs; 2.09–6.12 mmol g^{-1}).[45] For the amounts adsorbed at 298 K similar results were found.

As mentioned above, CO_2 uptakes depend on the surface area, the pore sizes and the interaction energy between a sorbent and a sorbate. The latter can be expressed by the heats of adsorption Q_{st} which we calculated for our materials (Fig. 5, bottom right). The values at the limit of zero coverage are shown in Table 1 and are the highest for *fl*-CTF300 and almost the same for the other *fl*-CTFs, ranging in the upper field compared to other POPs (see Table S7†).

For the use of *fl*-CTFs as potential flue gas sorbents the selectivities of CO_2 over N_2 need to be examined. Therefore, the Henry equation and the ideal adsorbed solution theory (IAST) were used (ESI, chapter 8†). The calculated values are listed in Table 1. As expected, *fl*-CTF300 and *fl*-CTF350 show the highest selectivities, due to the low adsorption potential towards argon compared to CO_2. The selectivities range in the upper level of POPs and, remarkably, *fl*-CTF300 shows a higher selectivity than FCTF-1.[16]

Motivated by the high values of adsorbed CO_2 at 273 K and the large number of micropores, we tested *fl*-CTF400 as a hydrogen storage material by carrying out hydrogen physisorption measurements at 77 K and 298 K up to 20 bar. The isotherm at 77 K is displayed in Fig. 6 and shows adsorption of 4.36 wt% (45.2 mmol g^{-1}), which is higher than that observed for 2D COFs (1.46–3.88 wt%, sat. pressure)[38] and polymers of intrinsic microporosity (PIMs, 1.45–2.71 wt%, 10 bar),[46–50] but

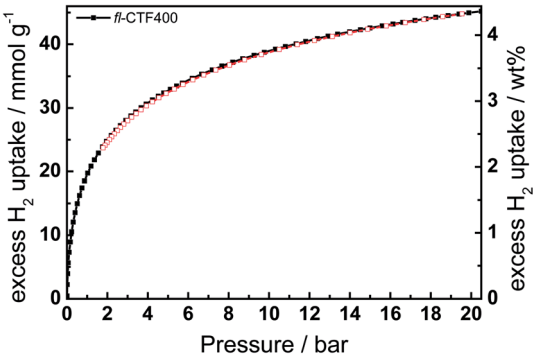

Fig. 6 Excess hydrogen adsorption (filled symbols) and desorption (open symbols) isotherm of *fl*-CTF400 at 77 K.

lower than that of the highly porous 3D COFs (6.98–7.16 wt%, sat. pressure),[38] PAFs (4.2–7.0 wt%)[51,52] and PPNs (8.34 wt%, 55 bar),[53] which however were measured at higher pressures. To date, only three CTFs were examined for their H_2 capacities and the measurements were done only up to 1 bar. CTF-1 adsorbs 1.55 wt%,[1] PCTF-1 1.86 wt%[11] and PCTF-2 0.9 wt%,[11] which is substantially lower than the uptake capacity of our material (1.95 wt%).

For hydrogen storage applications, knowledge of the heat of adsorption, along with the storage capacity, is of importance to better understand the microscopic host–guest interactions. Fig. S10† shows the temperature variations of the absolute hydrogen adsorption curves (77–117 K), which provides the strength of the binding potential for hydrogen in *fl*-CTF400. In Fig. S11,† the isosteric heat of adsorption is shown as a function of the surface coverage normalized to saturation coverage (20 bar, 77 K). Analysis of the hydrogen adsorption enthalpy gives a maximum value of 6.25 kJ mol^{-1} at near zero surface coverage, decreasing to 3.65 kJ mol^{-1} with increasing H_2 loading. The overall average heat of adsorption equals 4.9 kJ mol^{-1}. It is worth noting that the average heat of adsorption of 4.9 kJ mol^{-1} is relatively high after considering the rather large pore diameter (1.05–3 nm) and on comparison with most MOFs of similar pore sizes.[54] This relatively high average heat of adsorption can be either due to stronger adsorption sites (possibly N sites of *fl*-CTF400) or due to the ultramicropores inside *fl*-CTF400 as detected by CO_2 NLDFT simulations (0.35–1.45 nm). Table S5† summarizes the textural characteristics and hydrogen storage capacity of *fl*-CTF400.

Conclusions

The presented *fl*-CTFs were analyzed with respect to their local structure, porosity, and capacity for CO_2 capture. An intact fluorene network connected by triazines could be established for *fl*-CTF300. The materials showed high SAs up to 2862 $m^2 g^{-1}$ and high capacities for the adsorption of CO_2, which can be rationalized by their high fraction of ultramicropores. We find that *fl*-CTF350 with the highest fraction of micropores and moderate surface area shows the best CO_2 uptake (4.28 mmol g^{-1} at 273 K) and thus ranks in the upper level among all POPs.

Additionally, hydrogen adsorption of *fl*-CTF400 shows comparable values to other POPs. Finally, the gas selectivities of CO_2 over N_2 of the *fl*-CTFs were tested and reveal high values for *fl*-CTF300 and *fl*-CTF350, thus rendering these materials promising candidates for gas capture and storage.

Acknowledgements

The authors acknowledge financial support by the Deutsche Forschungsgemeinschaft, DFG (SPP 1362, SE 1417/5-1 and LO 1801/2-1), the Nanosystems Initiative Munich (NIM), the Center for Nanoscience (CeNS) and the Fonds der Chemischen Industrie (FCI). H. Oh was supported for this research through a stipend from the International Max Planck Research School for Advanced Materials (IMPRS-AM). We thank Marius Reymann and Niklas Cordes for synthetic assistance, Stephan Werner for XRD measurements, Christian Minke for ssNMR measurements and Katrin Rudolf and Christine Pösl for DTA/TG measurements. We acknowledge Prof. Thomas Bein and Prof. Wolfgang Schnick for access to the respective measurement facilities.

Notes and references

1 P. Kuhn, M. Antonietti and A. Thomas, *Angew. Chem., Int. Ed.*, 2008, **47**, 3450–3453.
2 P. Kuhn, A. l. Forget, D. Su, A. Thomas and M. Antonietti, *J. Am. Chem. Soc.*, 2008, **130**, 13333–13337.
3 P. Kuhn, A. Thomas and M. Antonietti, *Macromolecules*, 2009, **42**, 319–326.
4 P. Kuhn, A. Forget, J. Hartmann, A. Thomas and M. Antonietti, *Adv. Mater.*, 2009, **21**, 897–901.
5 S. Hug, M. E. Tauchert, S. Li, U. E. Pachmayr and B. V. Lotsch, *J. Mater. Chem.*, 2012, **22**, 13956–13964.
6 C. E. Chan-Thaw, A. Villa, P. Katekomol, D. Su, A. Thomas and L. Prati, *Nano Lett.*, 2010, **10**, 537–541.
7 R. Palkovits, M. Antonietti, P. Kuhn, A. Thomas and F. Schüth, *Angew. Chem., Int. Ed.*, 2009, **48**, 6909–6912.
8 C. E. Chan-Thaw, A. Villa, L. Prati and A. Thomas, *Chem. – Eur. J.*, 2011, **17**, 1052–1057.
9 P. Katekomol, J. Roeser, M. Bojdys, J. Weber and A. Thomas, *Chem. Mater.*, 2013, **25**, 1542–1548.
10 S. Ren, M. J. Bojdys, R. Dawson, A. Laybourn, Y. Z. Khimyak, D. J. Adams and A. I. Cooper, *Adv. Mater.*, 2012, **24**, 2357–2361.
11 A. Bhunia, V. Vasylyeva and C. Janiak, *Chem. Commun.*, 2013, **49**, 3961–3963.
12 X. Liu, H. Li, Y. Zhang, B. Xu, S. A, H. Xia and Y. Mu, *Polym. Chem.*, 2013, **4**, 2445–2448.
13 W. Wang, H. Ren, F. Sun, K. Cai, H. Ma, J. Du, H. Zhao and G. Zhu, *Dalton Trans.*, 2012, **41**, 3933–3936.
14 H. Ren, T. Ben, E. Wang, X. Jing, M. Xue, B. Liu, Y. Cui, S. Qiu and G. Zhu, *Chem. Commun.*, 2010, **46**, 291–293.
15 A. Bhunia, I. Boldog, A. Moller and C. Janiak, *J. Mater. Chem. A*, 2013, **1**, 14990–14999.
16 Y. Zhao, K. X. Yao, B. Teng, T. Zhang and Y. Han, *Energy Environ. Sci.*, 2013, **6**, 3684–3692.
17 X. Zhu, C. Tian, S. M. Mahurin, S.-H. Chai, C. Wang, S. Brown, G. M. Veith, H. Luo, H. Liu and S. Dai, *J. Am. Chem. Soc.*, 2012, **134**, 10478–10484.
18 M. R. Raupach, G. Marland, P. Ciais, C. Le Quéré, J. G. Canadell, G. Klepper and C. B. Field, *Proc. Natl. Acad. Sci. U. S. A.*, 2007, **104**, 10288–10293.
19 *Energy technology perspectives 2008*, International Energy Agency, Paris, 2008.
20 D. M. D'Alessandro, B. Smit and J. R. Long, *Angew. Chem., Int. Ed.*, 2010, **49**, 6058–6082.
21 R. Dawson, A. I. Cooper and D. J. Adams, *Polym. Int.*, 2013, **62**, 345–352.
22 R. S. Haszeldine, *Science*, 2009, **325**, 1647–1652.
23 G. T. Rochelle, *Science*, 2009, **325**, 1652–1654.
24 Z. Xiang and D. Cao, *J. Mater. Chem. A*, 2013, **1**, 2691–2718.
25 S.-Y. Ding and W. Wang, *Chem. Soc. Rev.*, 2013, **42**, 548–568.
26 R. Dawson, A. I. Cooper and D. J. Adams, *Prog. Polym. Sci.*, 2012, **37**, 530–563.
27 K. Sumida, D. L. Rogow, J. A. Mason, T. M. McDonald, E. D. Bloch, Z. R. Herm, T.-H. Bae and J. R. Long, *Chem. Rev.*, 2011, **112**, 724–781.
28 B. Streppel and M. Hirscher, *Phys. Chem. Chem. Phys.*, 2011, **13**, 3220–3222.
29 B. Streppel, PhD thesis, Universität Stuttgart, 2011.
30 M. Y. Wong and L. M. Leung, *Tetrahedron*, 2010, **66**, 3973–3977.
31 D. Vonlanthen, A. Rudnev, A. Mishchenko, A. Käslin, J. Rotzler, M. Neuburger, T. Wandlowski and M. Mayor, *Chem. – Eur. J.*, 2011, **17**, 7236–7250.
32 M. J. Bojdys, J. Jeromenok, A. Thomas and M. Antonietti, *Adv. Mater.*, 2010, **22**, 2202–2205.
33 V. G. Manecke and D. Wöhrle, *Makromol. Chem.*, 1968, **120**, 176–191.
34 M. R. Liebl and J. Senker, *Chem. Mater.*, 2013, **25**, 970–980.
35 K. S. W. Sing, D. H. Everett, R. A. W. Haul, L. Moscou, R. A. Pierotti, J. Rouquérol and T. Siemieniewska, *Pure Appl. Chem.*, 1985, **57**, 603–619.
36 S. Brunauer, P. H. Emmett and E. Teller, *J. Am. Chem. Soc.*, 1938, **60**, 309–319.
37 R. Dawson, E. Stockel, J. R. Holst, D. J. Adams and A. I. Cooper, *Energy Environ. Sci.*, 2011, **4**, 4239–4245.
38 H. Furukawa and O. M. Yaghi, *J. Am. Chem. Soc.*, 2009, **131**, 8875–8883.
39 G. Li and Z. Wang, *Macromolecules*, 2013, **46**, 3058–3066.
40 Y. Luo, S. Zhang, Y. Ma, W. Wang and B. Tan, *Polym. Chem.*, 2013, **4**, 1126–1131.
41 C. F. Martin, E. Stockel, R. Clowes, D. J. Adams, A. I. Cooper, J. J. Pis, F. Rubiera and C. Pevida, *J. Mater. Chem.*, 2011, **21**, 5475–5483.
42 M. G. Rabbani and H. M. El-Kaderi, *Chem. Mater.*, 2011, **23**, 1650–1653.
43 M. G. Rabbani and H. M. El-Kaderi, *Chem. Mater.*, 2012, **24**, 1511–1517.
44 M. G. Rabbani, A. K. Sekizkardes, O. M. El-Kadri, B. R. Kaafarani and H. M. El-Kaderi, *J. Mater. Chem.*, 2012, **22**, 25409–25417.

45 Y. Zhu, H. Long and W. Zhang, *Chem. Mater.*, 2013, **25**, 1630–1635.
46 N. B. McKeown, P. M. Budd and D. Book, *Macromol. Rapid Commun.*, 2007, **28**, 995–1002.
47 N. B. McKeown, B. Gahnem, K. J. Msayib, P. M. Budd, C. E. Tattershall, K. Mahmood, S. Tan, D. Book, H. W. Langmi and A. Walton, *Angew. Chem., Int. Ed.*, 2006, **45**, 1804–1807.
48 B. S. Gahnem, K. J. Msayib, N. B. McKeown, K. D. M. Harris, Z. Pan, P. M. Budd, A. Butler, J. Selbie, D. Book and A. Walton, *Chem. Commun.*, 2007, 67–69.
49 J.-Y. Lee, C. D. Wood, D. Bradshaw, M. J. Rosseinsky and A. I. Cooper, *Chem. Commun.*, 2006, 2670–2672.
50 P. M. Budd, A. Butler, J. Selbie, K. Mahmood, N. B. McKeown, B. Gahnem, K. Msayib, D. Book and A. Walton, *Phys. Chem. Chem. Phys.*, 2007, **9**, 1802–1808.
51 T. Ben, C. Pei, D. Zhang, J. Xu, F Deng, X. Jing and S. Qiu, *Energy Environ. Sci.*, 2011, **4**, 3991–3999.
52 T. Ben, H. Ren, S. Ma, D. Cao, J. Lan, X. Jing, W. Wang, J. Xu, F. Deng, J. M. Simmons, S. Qiu and G. Zhu, *Angew. Chem., Int. Ed.*, 2009, **48**, 9457–9460.
53 W. Lu, J. P. Sculley, D. Yuan, R. Krishna, Z. Wei and H.-C. Zhou, *Angew. Chem., Int. Ed.*, 2012, **51**, 7480–7484.
54 M. Schlichtenmayer and M. Hirscher, *J. Mater. Chem.*, 2012, **22**, 10134–10143.